

Distributed Integrated Sensing and Edge AI Exploiting Prior Information

Biao Dong, Bin Cao, *Member, IEEE*,
Guan Gui, *Fellow, IEEE*, and Qinyu Zhang, *Senior Member, IEEE*

Abstract—This work is concerned with a distributed integrated sensing and edge artificial intelligence (ISEA) system, where distributed devices perform target sensing and then offload locally estimated features to the access point (AP) for collaborative inference. The inference performance of this system is naturally determined by two levels: sensing and communication. We explore how priors can be exploited to enhance inference performance at both levels. At the sensing level, a Bayesian estimator under a Gaussian mixture (GM) prior is proposed, which yields the posterior by weighting class-conditional posterior with responsibilities. At the communication level, given a discriminative prior, optimal transceiver designs in terms of closed-form power allocation are derived for both time-division multiplexing (TDM) and frequency-division multiplexing (FDM) settings, revealing threshold-based and dual-decomposition structures. Experimental results verify that Bayesian estimator outperforms maximum likelihood (ML) at low SNR and discriminant-aware transceiver designs yield additional inference gains.

Index Terms—Edge artificial intelligence, distributed sensing, over-the-air computation, Bayesian estimation, Gaussian mixture prior.

I. INTRODUCTION

To support latency-sensitive applications such as smart factories, digital twins, and the low-altitude economy, the sixth generation (6G) of wireless networks is expected to extend its functional scope by integrating sensing capabilities, thereby giving rise to the paradigm of integrated sensing and communication (ISAC) [2]. In this fashion, massive sensory data needs to be processed in real time, which naturally involves three tightly coupled processes, namely sensing, communication, and computation, as illustrated in Fig. 1. From the computational perspective, intelligent computation is evolving toward an edge artificial intelligence (AI) assisted offloading architecture, which supports heterogeneous computing [3], specialized learning algorithms [4], and joint environmental perception with edge inference [5]. This architecture is referred to as integrated sensing and edge AI (ISEA) [6].

An efficient ISEA system relies on two key aspects: sensing-level enhancement and communication-level optimization [6].

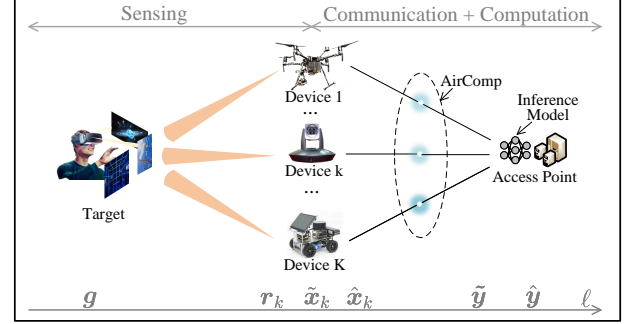


Fig. 1: The considered ISEA system consists of a single common target and one AP. Multiple devices first transmit probing signals for target sensing and then offload locally extracted features to the AP by AirComp.

The former aims to improve data quality from the sensing source through joint optimization of sensing error [7] and multi-view sensing aggregation [8]. The latter focuses on the cooperative multi-user communication, giving rise to a rich set of relevant techniques such as interference cancellation [9], time-slot and power allocation [10], and over-the-air computation (AirComp) [11]–[13]. A key design principle for both aspects is to enhance the inference performance by maximizing task-relevant semantic information, thereby shifting the focus from intrinsic observation to task-oriented design [6].

In view of this shift, both sensing and communication designs should incorporate task-relevant priors by modeling the parameter of interest as a random variable rather than a deterministic constant, as in classical maximum likelihood (ML) methods [14]. From the estimation-theoretic perspective, it corresponds to Bayesian estimation [14]. From the information-theoretic perspective, it can be interpreted as task-aware optimization given priors, such as maximizing semantic mutual information [15] or minimizing Bayes risk [16].

Within a Bayesian framework, existing ISEA studies adopt a Gaussian mixture (GM) prior at the sensing level and employ AirComp for multi-access aggregation at the communication level [7], [8], [17]. Specifically, [7] considered the sensing process with a GM prior and proposed a task-oriented AirComp framework for ISEA, where the Mahalanobis distance (MD) between two classes is adopted as a discriminant proxy for inference performance. This scheme was further proved to preserve the superior scaling law for max-value aggregation [17]. From an analytical perspective, [8] refined the multi-access process and compared AirComp with orthogonal multiple access (OMA). Their analysis demonstrates that AirComp

Parts of this paper were submitted to the IEEE International Conference on Communications (ICC), Glasgow, Scotland, May 2026 [1], which is available at: <https://arxiv.org/pdf/2510.21378>.

Biao Dong, Bin Cao and Qinyu Zhang are with the School of Electronic and Information Engineering, Harbin Institute of Technology (Shenzhen), Shenzhen 518055, China (e-mail: 23b952012@stu.hit.edu.cn; caobin@hit.edu.cn; zqy@hit.edu.cn).

Guan Gui is with the College of Telecommunications and Information Engineering, Nanjing University of Posts and Telecommunications, Nanjing 210003, China (e-mail: guiguan@njupt.edu.cn).

substantially outperforms OMA and achieves superior asymptotic scaling behavior, particularly when the number of receive antennas at the access point (AP) is limited [8].

ISEA remains in its infancy, and most existing studies do not properly exploit the prior information. While a GM prior is assumed, it is rarely incorporated explicitly into estimator design. Instead, these studies typically rely on the maximum likelihood (ML) estimator [7]–[10], [12], [17]. However, properly exploiting priors at the sensing stage is crucial, since the optimal estimator is inherently task-dependent, e.g., the Bayes-optimal estimator is the MMSE estimator under a squared error loss [14]. Furthermore, how to exploit priors at the communication level remains underexplored, due to the lack of a unified framework to characterize the relationship between task performance and AirComp error. Even with the introduction of task-aware proxies (e.g., MD in [7]), the performance gap between proxy-optimal and AirComp-optimal designs remains unclear.

Motivated by the aforementioned perspectives, this paper investigates a distributed ISEA system with the objective of maximizing inference performance, as illustrated in Fig. 1. Here, inference refers to determining the category given a specific sensing sample and represents a task-oriented classification process. The inference performance of this system is naturally determined by two levels: sensing and communication. We explore how priors can be exploited to enhance inference performance at both levels. The key contributions of this work are summarized as follows.

- We establish a unified framework that jointly exploits the prior information at both the sensing and communication levels. At the sensing level, we develop a responsibility-weighted Bayesian (RWB) estimator, which formulates the global posterior mean by weighting class-conditional posteriors with their associated responsibilities. At the communication level, we derive closed-form power allocation solutions for both TDM and FDM settings given discriminative priors, revealing threshold-based structures and a dual-decomposition interpretation.
- We provide theoretical insights at both sensing and communication levels. At the sensing level, the RWB estimator is interpreted using variational Bayes and conditional entropy. At the communication level, we characterize the relationship between AirComp aggregation error and classification performance, thereby providing a formal justification for two performance proxies, termed the computation-optimal and decision-optimal proxies. Furthermore, we explicitly establish the analytical connection between these two proxies.

The remainder of this paper is organized as follows. In Section II, the system model is presented. Section III introduces the RWB estimator and provides a theoretical analysis from the perspectives of variational Bayes and conditional entropy. In Section IV, we establish two performance proxies and subsequently derive the optimal transceiver designs for both TDM and FDM settings. Finally, Section V presents the numerical results, and Section VI concludes the paper.

Notations: Boldface letters denote vectors (e.g., \mathbf{x}). $\|\cdot\|^2$ denotes the squared Euclidean norm. $\mathcal{N}(\mu, \sigma^2)$ represents

the Gaussian distribution with mean μ and variance σ^2 . The superscript $(\cdot)^\top$ denotes the transpose operation. $H(\cdot)$, $H(\cdot|\cdot)$, and $H_b(\cdot)$ represent the entropy, conditional entropy, and binary entropy function, respectively. $\mathbf{I}_{a \times a}$ stands for the $a \times a$ identity matrix. $\text{KL}(\cdot \parallel \cdot)$ represents Kullback-Leibler (KL) divergence. Other major notations are summarized in Table I.

TABLE I: Summary of Major Notations.

Notation	Definition
$K/M/N/L$	Number of devices / features / subcarriers / categories
\mathbf{g}	Ground-truth data of the target
\mathbf{x}	Ground-truth feature
\mathbf{r}_k	Observed data of device k
$\tilde{\mathbf{x}}_k$	Noisy feature of device k
$\hat{\mathbf{x}}_k$	Estimated feature of device k
$b_{k,t} / b_{k,n}$	t -th slot or n -th subcarrier transmit coefficient of device k
$\tilde{y}_t / \tilde{y}_n$	t -th slot or n -th subcarrier received signal
a_t / a_n	t -th slot or n -th subcarrier receive coefficient
\hat{y}_t / \hat{y}_n	t -th slot or n -th subcarrier aggregated signal
\mathbf{v}	Class latent variable
σ_k^2	Sensing noise variance of device k
σ_m^2	Ground-truth feature variance at element m
$\hat{\sigma}_{k,t}^2 / \hat{\sigma}_{k,n}^2$	Estimated feature variance of device k transmitted on t -th slot or n -th subcarrier
π_ℓ	Mixing coefficients of class ℓ for GM
$\boldsymbol{\mu}_\ell$	Mean vector for class ℓ
$\boldsymbol{\Sigma}$	Covariance matrix for each class
θ_ℓ	Responsibility for class ℓ

II. SYSTEM MODEL

Consider a distributed ISEA system, as illustrated in Fig. 1. A set of K ISAC devices/users observe a common target for multi-view sensing. Each device performs local feature extraction based on its observations and transmits the estimated features to the AP over a multiple-access channel, thereby aggregating the features for collaborative inference. For simplicity, we consider that all the devices and the AP are equipped with a single antenna.

A. Sensing Model

1) *Sensing Process*: Each device, say device k , employs frequency-modulated continuous-wave (FMCW) modulation for target sensing, and the observation is denoted as [7], [18],

$$\mathbf{r}_k = \mathbf{g} + \mathbf{z}_k, \quad (1)$$

where $\mathbf{g} \in \mathbb{R}^F$ represents the ground-truth sensory data of the target, and $\mathbf{z}_k \sim \mathcal{N}(\mathbf{0}, \sigma_k^2 \mathbf{I}_{F \times F})$ denotes the *i.i.d.* AWGN. Here, F denotes the dimension of the received sensing signal, i.e., the number of time–frequency sampling points in a single FMCW frame.

2) *Feature Extraction*: The goal of the ISAC devices and the AP is to collaboratively infer the category of the target. Due to the bandwidth limitation, each observation \mathbf{r}_k must be compressed before transmission. Hence, we extract the

low-dimensional feature from \mathbf{r}_k using principal component analysis (PCA) as [19, Ch. 12]¹

$$\tilde{\mathbf{x}}_k = \mathbf{U}^\top \mathbf{r}_k = \underbrace{\mathbf{U}^\top \mathbf{g}}_{\text{Ground-truth } \mathbf{x}} + \underbrace{\mathbf{U}^\top \mathbf{z}_k}_{\text{Sensing noise } \mathbf{d}_k} = \mathbf{x} + \mathbf{d}_k, \quad (2)$$

where $\tilde{\mathbf{x}}_k \in \mathbb{R}^M$ is the observed feature vector processed by a unitary matrix $\mathbf{U} \in \mathbb{R}^{F \times M}$, consisting of the ground-truth feature \mathbf{x} and the sensing noise \mathbf{d}_k , and M denotes the feature dimension with $M \leq F$. Since the standard Gaussian distribution is unitary invariant, we have $\mathbf{d}_k \sim \mathcal{N}(\mathbf{0}, \sigma_k^2 \mathbf{I}_{M \times M})$. Then, each device performs local estimation based on (2) to obtain the estimated feature $\hat{\mathbf{x}}_k$. The specific estimator designs are detailed in Section III.

3) *Feature Distribution*: We model the feature vector $\mathbf{x} = [x_1, \dots, x_M]^\top$ in (2) as a Gaussian distribution for its analytical properties. Since the task-oriented classification involves multiple classes, a simple Gaussian distribution is insufficient to capture this complexity. We alternatively consider the GM, a superposition of L class-conditional Gaussians with prior mixing coefficients π_ℓ as

$$p(\mathbf{x}) = \sum_{\ell=1}^L \pi_\ell p(\mathbf{x}|\ell), \forall \ell \in \mathcal{L}, \quad (3)$$

where $\ell \in \mathcal{L} = \{1, \dots, L\}$, L denotes the number of total classes and $\sum_{\ell=1}^L \pi_\ell = 1$. Since the feature vector \mathbf{x} has M dimensions, it is modeled as an M -dimensional multivariate Gaussian distribution as

$$p(\mathbf{x}|\ell) = \mathcal{N}(\mathbf{x} | \boldsymbol{\mu}_\ell, \boldsymbol{\Sigma}), \quad (4)$$

where $\boldsymbol{\mu}_\ell = [\mu_{\ell,1}, \mu_{\ell,2}, \dots, \mu_{\ell,M}]^\top$ denotes the mean vector and $\boldsymbol{\Sigma} = \text{diag}(\sigma_1^2, \sigma_2^2, \dots, \sigma_M^2)$ denotes the diagonal covariance matrix.

Further, the distribution of the observed feature $\tilde{\mathbf{x}}_k$ can be derived. Since the sensing noise is *i.i.d.*, we have $p(\tilde{\mathbf{x}}_k|\ell) = \mathcal{N}(\tilde{\mathbf{x}}_k | \boldsymbol{\mu}_\ell, \tilde{\boldsymbol{\Sigma}})$, where $\tilde{\boldsymbol{\Sigma}} = \text{diag}(\tilde{\sigma}_{k,1}^2, \tilde{\sigma}_{k,2}^2, \dots, \tilde{\sigma}_{k,M}^2)$ with $\tilde{\sigma}_{k,m}^2 = \sigma_m^2 + \sigma_k^2$. The estimated feature $\hat{\mathbf{x}}_k$ is also modeled as a Gaussian $p(\hat{\mathbf{x}}_k|\ell) = \mathcal{N}(\hat{\mathbf{x}}_k | \hat{\boldsymbol{\mu}}_\ell, \hat{\boldsymbol{\Sigma}})$, where $\hat{\boldsymbol{\mu}}_\ell = [\hat{\mu}_{\ell,1}, \hat{\mu}_{\ell,2}, \dots, \hat{\mu}_{\ell,M}]^\top$ and $\hat{\boldsymbol{\Sigma}} = \text{diag}(\hat{\sigma}_{k,1}^2, \hat{\sigma}_{k,2}^2, \dots, \hat{\sigma}_{k,M}^2)$. Although the estimated feature in practice is not exactly Gaussian, a moment matching Gaussian approximation can be adopted [21].

Finally, the average receive sensing SNR SNR_s across the K devices is defined as

$$\text{SNR}_s = 10 \log_{10} \left(\frac{1}{K} \sum_{k=1}^K \frac{\frac{1}{M} \text{tr}(\boldsymbol{\Sigma})}{\sigma_k^2} \right),$$

which is normalized with respect to the transmit sensing power, consistent with [5, Eq. 6].

B. Multi-Access Model

For the ISEA system illustrated in Fig. 1, we adopt analog AirComp to transmit the estimated features $\hat{\mathbf{x}}_k$ to the AP. We begin by outlining the key assumptions regarding the AirComp. Based on these assumptions, we then introduce two

feature transmission schemes and the corresponding receiver aggregation procedure.

1) *Key Assumptions*: Key assumptions about channel are summarized as follows. First, a frequency-selective slow fading channel with a coherence duration of T_{cd} is considered for all devices. Second, each device operates in time-division duplex (TDD) mode and exploits channel reciprocity to acquire channel state information (CSI) [22, Ch. 5]. The time interval between uplink and downlink transmissions satisfies $\Delta t_{\text{TDD}} < T_{\text{cd}}$, ensuring that the channel remains constant during the TDD cycle. In addition, AirComp assumes that all devices transmit their signals synchronously and exploit the signal superposition property of the wireless multiple-access channel to accomplish a specific computation [12]. An example is the arithmetic mean, modeled as

$$\mathbf{y} = \frac{1}{K} \sum_{k=1}^K \hat{\mathbf{x}}_k, \quad (5)$$

where \mathbf{y} denotes the ideal received signal at the AP².

2) *Transmission Schemes*: To transmit the feature vector $\hat{\mathbf{x}}_k = [\hat{x}_{k,1}, \dots, \hat{x}_{k,M}]^\top$ within one coherence block, two transmission schemes are considered: TDM and FDM [23].

In the TDM scheme, each feature element is sequentially transmitted over M time slots. The received signal at the AP is

$$\tilde{y}_t = \sum_{k=1}^K h_{k,t} b_{k,t} \hat{x}_{k,t} + w_t, \quad t = 1, \dots, M, \quad (6)$$

where $b_{k,t}$ denotes the transmit coefficient over slot t at device k and $w_t \sim \mathcal{N}(0, \sigma_w^2)$ is the AWGN. We assume $M \leq T_{\text{cd}}$ and thus the channel coefficient $h_{k,t}$ remains constant, i.e. $h_{k,t} = h_k$.

In the FDM scheme, the feature elements are transmitted over N subcarriers ($M \leq N$). The received signal is

$$\tilde{y}_n = \sum_{k=1}^K h_{k,n} b_{k,n} \hat{x}_{k,n} + w_n, \quad n = 1, \dots, M,$$

where, with slight abuse of notation, $h_{k,n}$ denotes the channel response in frequency domain. Other notations follow the same definitions as the TDM scheme in (6). The received feature vector is $\tilde{\mathbf{y}} = [\tilde{y}_1, \tilde{y}_2, \dots, \tilde{y}_M]^\top$, and the transmit coefficients satisfy the total power constraint

$$\sum_{n=1}^M |b_{k,n}|^2 \nu_{k,n}^2 \leq P_k, \quad \nu_{k,n}^2 \triangleq \mathbb{E}[|\hat{x}_{k,n}|^2], \quad (7)$$

where $\nu_{k,n}^2$ can be estimated from offline training data samples [7], [8] and P_k denotes the power budget for device k . The communication SNR SNR_c is defined as [12]

$$\text{SNR}_c = 10 \log_{10} \left(\frac{P_k}{\sigma_w^2} \right).$$

3) *Receiver Aggregation*: Taking the FDM scheme as an example, the AP performs linear aggregation with the receive coefficient a_n as

$$\hat{\mathbf{y}}_n = a_n \tilde{y}_n = a_n \sum_{k=1}^K h_{k,n} b_{k,n} \hat{x}_{k,n} + a_n w_n. \quad (8)$$

¹Alternatively, neural networks can also be employed for feature extraction (see [20]). However, neural networks are analytically intractable due to their black-box nature.

²Common computation include averaging, maximum, and summation. Interested readers can refer to [6] and references therein.

The aggregated feature vector can be expressed as $\hat{\mathbf{y}} = [\hat{y}_1, \dots, \hat{y}_M]^\top$, which is subsequently fed into the classification model. The TDM case is analogous, obtained by replacing the subcarrier index n with time slot index t , as detailed in Table I.

Finally, the error introduced by AirComp, i.e., the mean squared error (MSE) between the ideal received signal defined in (5) and the aggregated feature vector defined in (8), is given by [12]

$$\mathbb{E}[\|\mathbf{e}\|^2] = \sum_{n=1}^M \underbrace{\left(\sum_{k=1}^K |a_n h_{k,n} b_{k,n} - 1|^2 \hat{\sigma}_{k,n}^2 + |a_n|^2 \sigma_w^2 \right)}_{\text{MSE}_n}, \quad (9)$$

where $\mathbf{e} \triangleq \hat{\mathbf{y}} - \mathbf{y}$ and MSE_n denotes the MSE of the n -th subcarrier in FDM, or equivalently, the t -th time slot (MSE_t) in TDM.

C. Classification Model

With the aggregated observation $\hat{\mathbf{y}}$ available, we formulate the subsequent inference task. Consider a standard supervised classification model with a training set $\mathcal{S} = \{(\mathbf{x}_i, \ell_i)\}_{i=1}^I$, where \mathbf{x}_i denotes the ground-truth features of the i -th observation defined in (2)³, ℓ_i represents the corresponding class label defined in (4) and the total number of sensed samples is I . The objective of training is to learn the mapping function (i.e., the classifier) $\ell = g(\mathbf{x})$, which maps input feature vectors to their corresponding class labels, based on the training set \mathcal{S} . Given prior mixing coefficients in (3), the theoretically optimal classifier follows the maximum a posteriori (MAP) rule as [19]

$$g^*(\mathbf{x}) = \arg \max_{\ell} \pi_{\ell} p(\mathbf{x} | \ell).$$

With the optimal classifier established, the inference reliability is formally quantified by the correct classification probability $\Pr(\ell | g(\mathbf{x}))$, which serves as the basis for final decision making.

The entire process from sensing to inference forms the following Markov chain

$$\mathbf{g} \rightarrow \mathbf{r}_k \rightarrow \tilde{\mathbf{x}}_k \rightarrow \hat{\mathbf{x}}_k \rightarrow \tilde{\mathbf{y}} \rightarrow \hat{\mathbf{y}} \rightarrow \ell, \quad (10)$$

as shown in Fig. 1. Based on this Markov chain, we observe that, with a fixed inference model, the task performance can only be improved from two levels: (i) enhancing the sensing quality ($\mathbf{g} \rightarrow \mathbf{r}_k \rightarrow \tilde{\mathbf{x}}_k \rightarrow \hat{\mathbf{x}}_k$), and (ii) reducing the communication error ($\hat{\mathbf{x}}_k \rightarrow \tilde{\mathbf{y}} \rightarrow \hat{\mathbf{y}}$). In the following sections, we investigate how priors can be exploited at both levels under a Bayesian philosophy.

III. PRIOR-AIDED SENSING SIGNAL ESTIMATION

In this section, we investigate the exploitation of prior information at the sensing level, aiming to estimate the truth vector \mathbf{x} from noisy observations $\tilde{\mathbf{x}}_k$, thereby contributing to the enhancement of downstream inference performance.

³In practice, the ground-truth features can be approximated by selecting high-SNR sensing segments.

A. Maximum Likelihood Estimation

The classical ML estimation treats the truth vector \mathbf{x} as a deterministic but unknown parameter [14]. Based on the observations in (2), the ML estimation of \mathbf{x} is

$$\hat{\mathbf{x}}_k^{\text{ML}} = \tilde{\mathbf{x}}_k, \quad (11)$$

where $\hat{\mathbf{x}}_k^{\text{ML}} = [\hat{x}_{k,1}^{\text{ML}}, \dots, \hat{x}_{k,M}^{\text{ML}}]^\top$. The element-wise MSE is

$$\text{MSE}_k^{\text{ML}} = \mathbb{E}[\|\hat{\mathbf{x}}_k^{\text{ML}} - \mathbf{x}_m\|^2] = \sigma_k^2, \forall m. \quad (12)$$

B. Bayesian Estimation

Different from ML estimation, Bayesian estimation treats \mathbf{x} as a random vector and aims at estimating its particular realization by MAP or minimum mean squared error (MMSE). Specifically, MAP estimation is

$$\hat{\mathbf{x}}_k^{\text{MAP}} = \arg \max_{\mathbf{x}} p(\mathbf{x} | \tilde{\mathbf{x}}_k) \stackrel{(a)}{=} \arg \max_{\mathbf{x}} p(\tilde{\mathbf{x}}_k | \mathbf{x}) p(\mathbf{x}), \quad (13)$$

while MMSE estimation is

$$\begin{aligned} \hat{\mathbf{x}}_k^{\text{MMSE}} &= \arg \min_{\hat{\mathbf{x}}} \mathbb{E}[\|\mathbf{x} - \hat{\mathbf{x}}\|^2 | \tilde{\mathbf{x}}_k] \\ &= \arg \min_{\hat{\mathbf{x}}} \int \|\mathbf{x} - \hat{\mathbf{x}}\|^2 p(\mathbf{x} | \tilde{\mathbf{x}}_k) d\mathbf{x} \\ &\stackrel{(b)}{=} \arg \min_{\hat{\mathbf{x}}} \int \|\mathbf{x} - \hat{\mathbf{x}}\|^2 p(\tilde{\mathbf{x}}_k | \mathbf{x}) p(\mathbf{x}) d\mathbf{x}, \end{aligned} \quad (14)$$

where (a) and (b) follow from Bayes' theorem: $p(\mathbf{x} | \tilde{\mathbf{x}}_k) \propto p(\tilde{\mathbf{x}}_k | \mathbf{x}) \times p(\mathbf{x})$, the likelihood function $p(\tilde{\mathbf{x}}_k | \mathbf{x})$ in (13) and (14) is determined by sensing model in (2) and $p(\mathbf{x})$ is the prior distribution given in (4). For a specific class ℓ , both $p(\tilde{\mathbf{x}}_k | \mathbf{x})$ and $p(\mathbf{x})$ are Gaussian. Within this Gaussian model, the MAP estimator coincides with the MMSE estimator, i.e., $\hat{\mathbf{x}}_k^{\text{MAP}} = \hat{\mathbf{x}}_k^{\text{MMSE}}$ [14, p. 358]. Hence, we focus on MMSE estimator below. Since the multiplication of two Gaussians is still a Gaussian, we have

$$p(\mathbf{x} | \tilde{\mathbf{x}}_k, \boldsymbol{\mu}_{\ell}, \boldsymbol{\Sigma}) = \mathcal{N}(\bar{\boldsymbol{\mu}}_{\ell}, \bar{\boldsymbol{\Sigma}}), \quad (15)$$

where

$$\begin{aligned} \bar{\boldsymbol{\mu}}_{\ell} &= \boldsymbol{\mu}_{\ell} + \boldsymbol{\Sigma}(\boldsymbol{\Sigma} + \sigma_k^2 \mathbf{I}_{M \times M})^{-1}(\tilde{\mathbf{x}}_k - \boldsymbol{\mu}_{\ell}), \\ \bar{\boldsymbol{\Sigma}} &= \boldsymbol{\Sigma} - \boldsymbol{\Sigma}(\boldsymbol{\Sigma} + \sigma_k^2 \mathbf{I}_{M \times M})^{-1} \boldsymbol{\Sigma}. \end{aligned}$$

In terms of each element, we have

$$\bar{\mu}_{\ell,m} = \frac{\sigma_m^2 \tilde{x}_{k,m} + \sigma_k^2 \mu_{\ell,m}}{\sigma_m^2 + \sigma_k^2}, \quad \bar{\sigma}_m^2 = \frac{\sigma_m^2 \sigma_k^2}{\sigma_m^2 + \sigma_k^2}. \quad (16)$$

Then, we can obtain the MMSE estimator as

$$\hat{\mathbf{x}}_k^{\text{MMSE}} = \frac{\sigma_m^2}{\sigma_m^2 + \sigma_k^2} \tilde{\mathbf{x}}_k + \frac{\sigma_k^2}{\sigma_m^2 + \sigma_k^2} \boldsymbol{\mu}_{\ell}, \quad (17)$$

The element-wise MSE is

$$\text{MSE}_k^{\text{MMSE}} = \mathbb{E}[\|\hat{\mathbf{x}}_k^{\text{MMSE}} - \mathbf{x}_m\|^2] = \frac{\sigma_m^2 \sigma_k^2}{\sigma_m^2 + \sigma_k^2}, \forall m. \quad (18)$$

By comparing (12) and (18), we observe that $\text{MSE}_k^{\text{MMSE}} \leq \text{MSE}_k^{\text{ML}}$ and equality holds only when the prior is non-informative (e.g., $\sigma_m^2 \rightarrow \infty$).

In practice, the optimal $\text{MSE}_k^{\text{MMSE}}$ relies on $\boldsymbol{\mu}_{\ell}$ as (17). However, exploiting a well-calibrated prior for the class means is challenging, see the following Remark.

Remark 1. Since the true class varies across observations, the class-conditional prior in (4) can be invoked in (17)

only when μ_ℓ is known. μ_ℓ depends on label ℓ , which is unknown at each device and is instead inferred at the AP via collaborative inference, as shown in Fig. 1. Each device only retains the offline-estimated statistics over all classes, i.e., $\{\mu_\ell\}_{\ell=1}^L$. Therefore, the exact MMSE estimation (17) is not computable by each device. This motivates estimating the responsibility that the observation belongs to each class, and deriving an RWB estimator.

C. Responsibility-Weighted Bayesian Estimation

1) *The Latent Variables Model:* Before introducing the RWB estimator, we reformulate the feature distribution in Section II-A3 from the perspective of *latent variables*⁴. Specifically, the class label ℓ and the ground-truth feature \mathbf{x} are modeled as the latent variables, as shown in Fig. 2(a). Define a one-hot-coded random vector $\mathbf{v} = [v_1, \dots, v_L]^\top$ with $v_\ell = 1$ for the true class and $v_{\ell'} = 0$ for $\ell' \neq \ell$, where $(\ell, \ell') \in \mathcal{L}$ defined in (3). Then, we rewrite (3) with \mathbf{v} as

$$p(\mathbf{x} | \mathbf{v}) = \prod_{\ell=1}^L \mathcal{N}(\mathbf{x} | \mu_\ell, \Sigma)^{v_\ell}.$$

With the observation $\tilde{\mathbf{x}}_k$, the joint distribution can be factorized as

$$p(\tilde{\mathbf{x}}_k, \mathbf{x}, \mathbf{v}) = p(\tilde{\mathbf{x}}_k | \mathbf{x})p(\mathbf{x} | \mathbf{v})p(\mathbf{v}),$$

where $p(\mathbf{v}) = \prod_{\ell=1}^L \pi_\ell^{v_\ell}$ and $p(\tilde{\mathbf{x}}_k | \mathbf{x}) = \mathcal{N}(\tilde{\mathbf{x}}_k | \mathbf{x}, \sigma_k^2 \mathbf{I})$. Further, the class-conditional likelihood $\tilde{\mathbf{x}}_k$ given \mathbf{v} is

$$\begin{aligned} p(\tilde{\mathbf{x}}_k | v_\ell=1) &= \int p(\tilde{\mathbf{x}}_k | \mathbf{x})p(\mathbf{x} | v_\ell=1)d\mathbf{x} \\ &= \int \mathcal{N}(\tilde{\mathbf{x}}_k | \mathbf{x}, \sigma_k^2 \mathbf{I})\mathcal{N}(\mathbf{x} | \mu_\ell, \Sigma)d\mathbf{x} \\ &= \mathcal{N}(\tilde{\mathbf{x}}_k | \mu_\ell, \Sigma + \sigma_k^2 \mathbf{I}), \end{aligned} \quad (19)$$

where the corresponding variable dependencies are illustrated in Fig. 2(a).

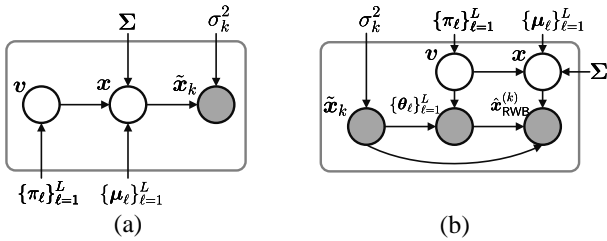


Fig. 2: Two graphical models, where white nodes denote latent variables, gray nodes denote observed variables, and arrows indicate conditional dependencies.

2) *Details of the RWB Estimator:* The exact MMSE estimation relies on the priors for specific class means, which is unknown at each device, as stated in Remark 1. Hence, we adopt an RWB estimator that scales the estimate using all class-mean priors with the observation. The corresponding variable dependencies of RWB are illustrated in Fig. 2(b) and defined below.

⁴Gaussian mixture in (3) can be interpreted via discrete latent variables [19, Ch. 9], where the latent variables can be interpreted as the assignment of each observation to a particular mixture component, which often can not be observed.

Definition 1. Based on (19), the responsibility θ_ℓ is defined as the posterior probability of the latent variable v_ℓ

$$\theta_\ell = p(v_\ell=1 | \tilde{\mathbf{x}}_k) \stackrel{(a)}{=} \frac{\pi_\ell \mathcal{N}(\tilde{\mathbf{x}}_k | \mu_\ell, \Sigma + \sigma_k^2 \mathbf{I})}{\sum_{j=1}^L \pi_j \mathcal{N}(\tilde{\mathbf{x}}_k | \mu_j, \Sigma + \sigma_k^2 \mathbf{I})}, \quad (20)$$

where (a) follows from Bayes' theorem.

By expanding the Gaussian density function in Definition 1, we observe that

$$\theta_\ell \propto \pi_\ell \exp\left(-\frac{1}{2}(\tilde{\mathbf{x}}_k - \mu_\ell)^\top (\Sigma + \sigma_k^2 \mathbf{I})^{-1} (\tilde{\mathbf{x}}_k - \mu_\ell)\right).$$

For a fixed σ_k^2 and $\tilde{\mathbf{x}}_k$, the responsibility θ_ℓ measures how close the observation is to the ℓ -th class mean μ_ℓ . In other words, it quantifies the likelihood of each class and is typically used for estimating the mixing coefficients of GM, such as Expectation-Maximisation (EM) algorithm [24]. Since each device retains the offline-estimated statistics over all classes, the posterior in (15) can be reformulated as a GM weighted by the θ_ℓ , i.e.,

$$p(\mathbf{x} | \tilde{\mathbf{x}}_k, \{\mu_\ell\}_{\ell=1}^L, \Sigma) = \sum_{\ell=1}^L \theta_\ell \mathcal{N}(\mathbf{x} | \bar{\mu}_\ell, \bar{\Sigma}). \quad (21)$$

By moment matching [21], (21) can be approximated by a single Gaussian

$$p(\mathbf{x} | \tilde{\mathbf{x}}_k, \{\mu_\ell\}_{\ell=1}^L, \Sigma) \approx \mathcal{N}(\bar{\mu}, \bar{\Sigma}), \quad (22)$$

where

$$\bar{\mu} = \sum_{\ell=1}^L \theta_\ell \bar{\mu}_\ell, \quad \bar{\Sigma} = \sum_{\ell=1}^L \theta_\ell [\bar{\Sigma} + (\bar{\mu}_\ell - \bar{\mu})(\bar{\mu}_\ell - \bar{\mu})^\top].$$

In terms of each element, we have

$$\bar{\mu}_m = \sum_{\ell=1}^L \theta_\ell \bar{\mu}_{\ell,m}, \quad \bar{\sigma}_m^2 = \bar{\sigma}_m^2 + \sum_{\ell=1}^L \theta_\ell (\bar{\mu}_{\ell,m} - \bar{\mu}_m)^2. \quad (23)$$

Then, we can rewrite (17) as

$$\hat{\mathbf{x}}_k^{\text{RWB}} = \sum_{\ell=1}^L \theta_\ell \left[\frac{\sigma_m^2}{\sigma_m^2 + \sigma_k^2} \tilde{\mathbf{x}}_k + \frac{\sigma_k^2}{\sigma_m^2 + \sigma_k^2} \mu_\ell \right]. \quad (24)$$

The element-wise MSE is

$$\text{MSE}_k^{\text{RWB}} = \mathbb{E}[|\hat{x}_{k,m}^{\text{RWB}} - x_m|^2] = \bar{\sigma}_m^2 + \sum_{\ell=1}^L \theta_\ell (\bar{\mu}_{\ell,m} - \bar{\mu}_m)^2, \quad \forall m, \quad (25)$$

where $\bar{\sigma}_m^2$ denotes the within-class uncertainty achieved by the exact MMSE estimation (17) and $\sum_{\ell=1}^L \theta_\ell (\bar{\mu}_{\ell,m} - \bar{\mu}_m)^2$ denotes the between-class uncertainty controlled by θ_ℓ . By comparing (25) and (18), we observe $\text{MSE}_k^{\text{MMSE}} \leq \text{MSE}_k^{\text{RWB}}$ and equality holds only when between-class uncertainty vanishes to 0. The overall procedure of RWB estimator is summarized in Algorithm 1.

3) *Variational Analysis of the RWB Estimator:* To gain further insight, we analyse the RWB estimator from the perspective of variational Bayes [19, Ch. 10]. Let $\boldsymbol{\eta} \triangleq \{\{\mu_\ell\}_{\ell=1}^L, \Sigma, \{\pi_\ell\}_{\ell=1}^L\}$ denotes all model parameters and let $\boldsymbol{\omega} \triangleq \{\mathbf{v}, \mathbf{x}\}$ collects all latent variables. Our goal is to estimate the truth vector \mathbf{x} from noisy observations $\tilde{\mathbf{x}}_k$ given prior $\boldsymbol{\eta}$, which can be formulated as

$$\hat{\mathbf{x}}_k^{\text{RWB}} = \arg \min_{\hat{\mathbf{x}}} \mathbb{E}[\|\mathbf{x} - \hat{\mathbf{x}}\|^2 | \tilde{\mathbf{x}}_k, \boldsymbol{\eta}] = \mathbb{E}[\mathbf{x} | \tilde{\mathbf{x}}_k, \boldsymbol{\eta}]. \quad (26)$$

When $\boldsymbol{\eta}$ is unknown and must be learned, we typically

Algorithm 1 Responsibility-Weighted Bayesian Estimation

- 1: **Input:** $\{\mu_\ell\}_{\ell=1}^L$, Σ , $\{\pi_\ell\}_{\ell=1}^L$, σ_k^2 , and \tilde{x}_k .
 - 2: **(Per-class likelihood)** Compute the class-conditional likelihoods using (19).
 - 3: **(Responsibilities)** For each ℓ , compute the class responsibilities via (20).
 - 4: **(RWB aggregation)** Compute the responsibility-weighted Bayesian estimate using (24).
 - 5: **Output:** \hat{x}_k^{RWB} .
-

maximize the marginal likelihood as

$$p(\tilde{x}_k | \eta) = \int p(\tilde{x}_k, \omega | \eta) d\omega, \quad (27)$$

which is often intractable due to the high-dimensional integration over ω . A variational distribution $q(\omega)$ is introduced to approximate $p(\omega | \tilde{x}_k, \eta)$ in variational Bayes [19, Ch. 10], and the approximation is quantified by the KL divergence as $\text{KL}(q(\omega) || p(\omega | \tilde{x}_k, \eta))$. Then, rewriting (27) as log likelihood with $q(\omega)$ yields

$$\begin{aligned} \log p(\tilde{x}_k | \eta) &= \log \int q(\omega) \frac{p(\tilde{x}_k, \omega | \eta)}{q(\omega)} d\omega \\ &\stackrel{(a)}{\geq} \int q(\omega) \log \frac{p(\tilde{x}_k, \omega | \eta)}{q(\omega)} d\omega \triangleq \mathcal{Q}(q, \eta), \end{aligned} \quad (28)$$

where (a) follows from Jensen's inequality, equality holds only when the optimal variational distribution equals the true posterior, i.e., $\text{KL}(q(\omega) || p(\omega | \tilde{x}_k, \eta)) = 0$ and $\mathcal{Q}(q, \eta)$ denotes a functional with respect to $q(\omega)$. The exact decomposition of (28) can be derived as

$$\log p(\tilde{x}_k | \eta) = \mathcal{Q}(q, \eta) + \text{KL}(q(\omega) || p(\omega | \tilde{x}_k, \eta)). \quad (29)$$

By comparing (29) and (26), we observe that when η is fixed, the posterior responsibility is obtained exactly as

$$\theta_\ell = q(v_\ell=1) = p(v_\ell=1 | \tilde{x}_k, \eta). \quad (30)$$

Substituting θ_ℓ and $p(x | \tilde{x}_k, \eta)$ into (26) yields the RWB estimator.

Remark 2. The performance of the RWB estimator is sensitive to the quality of the θ_ℓ , which depends on the accuracy of the offline-estimated class statistics and sensing noise variance. In our implementation, η is computed from a large labeled dataset and σ_k^2 is treated as a tunable hyper-parameter. These practices ensure that the resulting θ_ℓ serves as robust approximations of MMSE estimator, as shown in Fig. 3. In the following aggregation analysis, we thus focus on the aggregation performance of MMSE estimator.

D. Aggregation Analysis

Given the specific estimator designs, we now investigate their impact on the aggregation gain. Since the receiver is only interested in the specific computation as (5), we analyze the aggregation performance in terms of the entropy of the aggregated random variable under different estimators. For simplicity, we consider noise-free aggregation without fading or noise and focus on the aggregation of a single feature dimension, i.e., $y_m = \frac{1}{K} \sum_{k=1}^K \hat{x}_{k,m}$, and omit the subscript m in the following for notation simplicity.

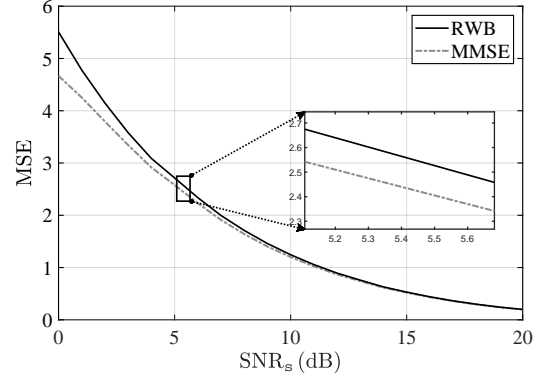


Fig. 3: MSE versus sensing SNR under ML estimation and the proposed RWB estimation. In this figure, AirComp aggregation is assumed noise-free. The MMSE curve corresponds to the theoretical performance under known class labels and thus serves as a lower bound.

When each device adopts the ML estimator in (12), the fundamental limit of the achievable aggregation gain is characterized by the conditional entropy [25, Ch. 8]

$$\begin{aligned} H(x | y^{\text{ML}}) &= \frac{1}{2} \log \left(2\pi e \left[\frac{1}{\sigma^2} + \frac{K^2}{\sum_{k=1}^K \sigma_k^2} \right]^{-1} \right) \quad (31) \\ &\stackrel{(a)}{\geq} \frac{1}{2} \log \left(2\pi e \left[\frac{1}{\sigma^2} + \sum_{k=1}^K \frac{1}{\sigma_k^2} \right]^{-1} \right). \end{aligned}$$

where $y^{\text{ML}} = \frac{1}{K} \sum_{k=1}^K \hat{x}_k^{\text{ML}}$, (a) follows from the Cauchy-Schwarz inequality and equality holds only when all devices have identical sensing noise variances, i.e., $\sigma_1^2 = \dots = \sigma_K^2$. Further, if each device adopts the MMSE estimator in (24), the conditional entropy is

$$H(x | y^{\text{MMSE}}) = \frac{1}{2} \log \left(2\pi e \left[\frac{1}{\sigma^2} + \frac{(\sum_{k=1}^K \varrho_k)^2}{\sum_{k=1}^K \varrho_k^2 \sigma_k^2} \right]^{-1} \right), \quad (32)$$

where $y^{\text{MMSE}} = \frac{1}{K} \sum_{k=1}^K \hat{x}_k^{\text{MMSE}}$ and $\varrho_k = \frac{\sigma^2}{\sigma^2 + \sigma_k^2}$. By comparing (31) and (32), we can obtain the following insights:

- Two conditional entropies are structurally equivalent and only differ in the effective noise variance term, i.e., $\frac{K^2}{\sum_{k=1}^K \sigma_k^2}$ and $\frac{(\sum_{k=1}^K \varrho_k)^2}{\sum_{k=1}^K \varrho_k^2 \sigma_k^2}$.
- When the prior becomes non-informative (i.e., $\sigma^2 \rightarrow \infty$, which implies $\varrho_k \rightarrow 1$), we have $H(x | y^{\text{MMSE}}) \approx H(x | y^{\text{ML}})$.
- When the prior is informative, we have $H(x | y^{\text{MMSE}}) \leq H(x | y^{\text{ML}})$, which follows Chebyshev's sum inequality and equality holds only when all devices have identical sensing noise variances [26, p. 43].

Based on the above analysis, we can conclude that exploiting the prior information at the sensing level reduces the conditional entropy of the aggregated signal and reverts to the ML under the non-informative prior regime. The above discussion assumes a noise-free AirComp aggregation. In the following, we further consider noisy aggregation, and investigate how to exploit priors at the communication level.

IV. PRIOR-AIDED AIRCOMP TRANSCEIVER DESIGN

In this section, we study how to exploit the prior knowledge at the communication level. Specifically, two proxies, namely

the computation-optimal and decision-optimal proxies, are introduced to quantify the impact of AirComp on classification performance, both based on prior-driven structures. Second, building on the two proxies, we further derive the optimal transceiver designs for AirComp under both TDM and FDM settings.

A. Two Proxies

1) *Computation-Optimal Proxy*: The computation-optimal proxy is built upon the concept of the *classification margin* γ [17], [27], which establishes a bridge between the classification accuracy and the AirComp error (9)⁵.

Theorem 1 ([17], [27]). *The classification accuracy at the AP is lower bounded as*

$$A_{AP} \geq A_0 \Pr[||e|| < \gamma] \stackrel{(a)}{\geq} A_0 \left(1 - \frac{\mathbb{E}[||e||^2]}{\gamma^2}\right),$$

where A_0 denotes the classification performance of the inference model $g(\cdot)$ under noise-free transmission and (a) follows the Markov's inequality.

Theorem 1 implies that a sufficient condition for correct classification is that the statistical error introduced by AirComp must be sufficiently small. Since γ is fixed for a given classification model, minimizing the computation MSE in (9) contributes to improved classification accuracy.

2) *Decision-Optimal Proxy*: The decision-optimal proxy is developed from the perspective of Bayesian hypothesis testing, which establishes a connection between MD and classification accuracy.

Theorem 2. *The MAP estimator achieves the minimum error probability in classifying \mathbf{x} , and the corresponding classification error probability asymptotically behaves as*

$$P_e \doteq \exp(-\kappa K G_{\min}), \quad (33)$$

where \doteq denotes equivalence in exponential order, κ is the constant coefficient and G_{\min} is the minimum inter-class MD between any two classes.

Proof. First, the classification error probability P_e of any classifier is lower bounded by Fano's inequality as [28]

$$H(\ell|\mathbf{x}) \leq H_b(P_e) + P_e \log(|\mathcal{L}| - 1), \quad (34)$$

where $P_e \triangleq 1 - \Pr(\ell | g(\mathbf{x}))$ and $|\mathcal{L}|$ is the cardinality of the set \mathcal{L} . For sufficiently large observations, we have the following asymptotic relationship [28]

$$H(\ell|\mathbf{x}) \doteq P_e \doteq \exp(-KC), \quad (35)$$

where $C = \min_{0 \leq \rho \leq 1} D_{\text{ch}}(p(\mathbf{x}|\ell) \| p(\mathbf{x}|\ell')), \forall (\ell, \ell') \in \mathcal{L}$ denotes the minimum Chernoff information over all the possible class pairs, achieved by optimizing the parameter ρ in the Chernoff distance $D_{\text{ch}}(\cdot \| \cdot)$ [29, p. 98]. Under the identical class covariances Σ (see (4)), the Bhattacharyya distance coincides with the optimal Chernoff distance when $\rho = 1/2$, and can be further simplified as

$$C = \kappa G_{\min}, \quad (36)$$

⁵The classification margin is an intrinsic property of a classifier, representing an inherent separation in the feature space.

where $G_{\min} = \min_{(\ell, \ell') \in \mathcal{L}} G_{\ell, \ell'}(\mathbf{x})$ is the minimum inter-class MD between any two classes and $G_{\ell, \ell'}(\mathbf{x})$ is given in Definition 2. By substituting (36) into (35), we have (33). ■

Definition 2. *The MD between classes ℓ and ℓ' is defined via the symmetric KL divergence as [30]*

$$G_{\ell, \ell'}(\mathbf{x}) = \text{KL}(p(\mathbf{x}|\ell) \| p(\mathbf{x}|\ell')) + \text{KL}(p(\mathbf{x}|\ell') \| p(\mathbf{x}|\ell)) \\ \stackrel{(a)}{=} (\boldsymbol{\mu}_\ell - \boldsymbol{\mu}_{\ell'})^\top \boldsymbol{\Sigma}^{-1} (\boldsymbol{\mu}_\ell - \boldsymbol{\mu}_{\ell'}) \stackrel{(b)}{=} \sum_{m=1}^M G_{\ell, \ell'}(x_m), \quad (37)$$

where $p(\mathbf{x}|\ell)$ is given in (4), $G_{\ell, \ell'}(x_m) \triangleq \frac{(\mu_{\ell, m} - \mu_{\ell', m})^2}{\sigma_m^2}$, (a) uses the fact that both classes share the same covariance Σ , and (b) follows from the diagonal form of the covariance after PCA, which makes the feature dimensions statistically independent.

Theorem 2 suggests that aggregating sufficient independent observations mitigates class uncertainty, thereby yielding improved classification performance. Similarly, maximizing the inter-class MD also leads to uncertainty reduction and enhanced separability. Notably, MD acts as a metric proxy since it satisfies the four axioms of a metric space [31, p. 3]. Guided by these two proxies, we now derive the optimal transceiver designs in terms of closed-form power allocation for AirComp under both TDM and FDM settings.

B. TDM Setting

1) *Computation-Optimal Case*: Under the computation-optimal case, the optimization problem can be formulated as

$$(P1) \quad \min_{\{b_{k,t}, a_t\}_{t=1}^M} \sum_{t=1}^M \text{MSE}_t, \quad \text{s.t. (7).}$$

where MSE_t can be derived by (9). This formulation is Bayesian in that the class statistic $\hat{\sigma}_m^2$ is treated as prior learned offline.

Since the channel is slow fading (i.e., $h_{k,t} = h_k$, $b_{k,t} = b_k$, $\nu_{k,t} = \nu_k$, $\hat{\sigma}_{k,t}^2 = \hat{\sigma}_k^2$ and $a_t = a$), (P1) reduces to independent per-slot optimizations as

$$(P2) \quad \min_{b_k, a} \text{MSE}_t, \quad \text{s.t. } |b_k|^2 \nu_k^2 \leq P_k.$$

(P2) has an optimal solution, as stated in the following theorem.

Theorem 3 ([12], [13]). *Assuming $P_1|h_1| \leq \dots \leq P_K|h_K|$, the optimal solution of (P2) is*

$$|b_k^*| = \begin{cases} \frac{\sqrt{P_k}}{|\nu_k|}, & 1 \leq k \leq k^*, \\ \frac{1}{|a^*||h_k|}, & k^* < k \leq K, \end{cases} \quad (38)$$

where $a^* = \frac{\sum_{k=1}^{k^*} |h_k| \hat{\sigma}_k^2 \sqrt{P_k} / |\nu_k|}{\sum_{k=1}^{k^*} |h_k|^2 \hat{\sigma}_k^2 P_k / |\nu_k|^2 + \sigma_w^2}$ and k^* denotes the threshold index that separates the full-power and channel-inversion transmission.

2) *Decision-Optimal Case*: Unlike the computation-optimal case, the decision-optimal case aims to maximize the inter-class MD $G_{\ell, \ell'}(\mathbf{x})$, as defined in (37). The decision-optimal formulation can also be optimized independently

across different time slots. To this end, we first derive the expression of MD for each received feature element and then formulate the optimization problem.

Based on (8) and (37), the MD of the m -th received feature element can be expressed as

$$G_{\min}(\hat{y}_m) = \min_{(\ell, \ell') \in \mathcal{L}} G_{\ell, \ell'}(\hat{y}_m) = \frac{|\sum_{k=1}^K h_k b_k|^2 \Delta_m}{\sum_{k=1}^K |h_k b_k|^2 \hat{\sigma}_{k,m}^2 + \sigma_w^2}, \quad (39)$$

where $\Delta_m \triangleq \min_{(\ell, \ell') \in \mathcal{L}} (\mu_{\ell, m} - \mu_{\ell', m})^2$ can be viewed as a discriminative prior and estimated from offline training data. Meanwhile, it can be observed that the MD is independent of a . Hence, the optimization focuses on the b_k , as formulated below.

$$(P3) \max_{b_k} \quad (39), \quad \text{s.t. } |b_k|^2 \nu_k^2 \leq P_k.$$

Remark 3. This modeling is also Bayesian in that Δ_m and $\mu_{\ell, m}$ are treated as priors learned offline. In this regard, (39) is a prior-informed objective rather than a purely likelihood-based one.

(P3) has an optimal solution, which is given in the following theorem.

Theorem 4. The optimal solution to problem (P3) exhibits a threshold-based structure, given by

$$|b_k^*| = \begin{cases} \frac{\sqrt{P_k}}{|\nu_k|}, & u_k \leq \tau^*, \\ \frac{\tau^*}{|h_k|}, & u_k > \tau^*, \end{cases} \quad (40)$$

where $u_k \triangleq \frac{|h_k| \sqrt{P_k}}{\nu_k}$ and τ^* denotes the capping threshold.

Proof. Define $\Delta' = \frac{|\Delta_m|^2}{\hat{\sigma}_m^2}$, $\sigma_{\text{eq}}^2 = \frac{\sigma_w^2}{\hat{\sigma}_m^2}$, $c_k \triangleq |h_k| |b_k|$ and $u_k \triangleq \frac{|h_k| \sqrt{P_k}}{\nu_k}$. Without loss of generality, we assume $u_1 \leq \dots \leq u_K$. Then, (P3) can be equivalently reformulated as

$$(P4) \max_{c_k} F(\mathbf{c}) = \frac{\Delta' (\sum_{k=1}^K c_k)^2}{\sum_{k=1}^K c_k^2 + \sigma_{\text{eq}}^2}, \quad \text{s.t. } 0 \leq c_k \leq u_k, \quad \forall k.$$

(P4) is a fractional programming problem [32]. Define $\sum_{k=1}^K c_k = S_1$. Since the denominator of $F(\mathbf{c})$ is a convex function, (P4) can be readily verified to be equivalent to

$$(P5) \min_{\{c_k\}} \sum_{k=1}^K c_k^2, \quad \text{s.t. } \sum_{k=1}^K c_k = S_1, \quad 0 \leq c_k \leq u_k, \quad \forall k.$$

(P5) is a quadratic programming problem [32], whose Lagrangian can be expressed as

$$\mathcal{L}_{P5} = \sum_{k=1}^K c_k^2 - \lambda \left(\sum_{k=1}^K c_k - S_1 \right) + \sum_{k=1}^K \alpha_k (c_k - u_k) - \sum_{k=1}^K \beta_k c_k,$$

where λ , α_k , and β_k denote the Lagrange multipliers. According to the Karush–Kuhn–Tucker (KKT) conditions [32], the optimal solution satisfies

$$c_k^* = \min\{u_k, \tau\}, \quad \tau = \lambda/2 \geq 0,$$

which exhibits a threshold-based structure, where weaker links (i.e., smaller u_k) saturate first. Without loss of generality, we

assume that the first j links are saturated, while the remaining $(K - j)$ links share a common capping threshold τ , i.e.,

$$c_k = \begin{cases} u_k, & 1 \leq k \leq j, \\ \tau, & j < k \leq K. \end{cases} \quad (41)$$

By substituting (41) into $F(\mathbf{c})$, we have $F(\tau) = \frac{\Delta' (\sum_{k=1}^j u_k + (K-j)\tau)^2}{(\sum_{k=1}^j u_k^2) + (K-j)\tau^2 + \sigma_{\text{eq}}^2}$. Checking the first derivative of $F(\tau)$ yields the stationary point

$$\tau_j = \frac{\sum_{k=1}^j u_k^2 + \sigma_{\text{eq}}^2}{\sum_{k=1}^j u_k}, \quad j \geq 1.$$

If $\tau_j \in (u_j, u_{j+1})$, it serves as the unique maximizer of $F(\tau)$ within this segment. Otherwise, the segment-wise optimum occurs at the boundary, i.e., $\tau = u_j$ or $\tau = u_{j+1}$. By comparing all segments, the global threshold τ^* can be obtained. Accordingly, the optimal c_k^* values are determined, and the corresponding transmit amplitudes $|b_k^*|$ can be obtained as (40). ■

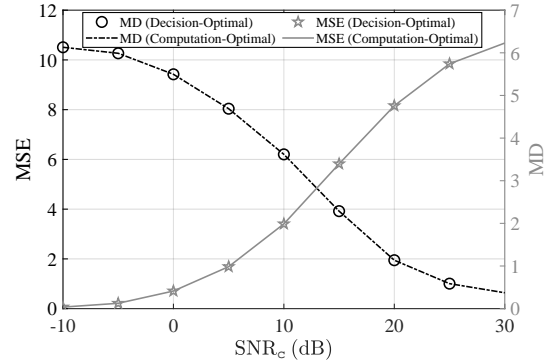


Fig. 4: MSE and MD versus the communication SNR under MSE-optimal and decision-optimal designs in the TDM setting.

Remark 4. By comparing (40) and (38), we observe that both proxies yield the similar optimal solution structure. The resulting MSE and MD performances are also identical, as illustrated in Fig. 4. The underlying reason is that, in the TDM scheme, the temporal degree of freedom (DoF) do not provide additional gain, since all slots experience the same quasi-static channel realization. Despite known discriminative prior Δ_m , the lack of slot heterogeneity makes it impossible to allocate resources across slots according to discriminative features. In this regard, irrespective of the chosen proxy, the resulting solution exhibits the same structural form.

We notice that the discriminative prior is heterogeneous across feature dimensions. To better utilize this prior, it is beneficial for the channel DoF to support corresponding multiplexing, enabling non-uniform resource allocation that aligns with feature importance. We now extend this analysis to the FDM case.

C. FDM Setting

1) *Computation-Optimal Case:* Different from (P1), each feature element here is transmitted over different subcarriers

rather than different time slots. Due to the frequency-selective channel, a joint power constraint across all subcarriers should be considered. The corresponding optimization problem can be formulated as

$$(P6) \quad \min_{\{b_{k,n}, a_n\}_{n=1}^M} \sum_{n=1}^M \text{MSE}_n, \quad \text{s.t. (7).}$$

(P6) is non-convex due to the coupling between $b_{k,n}$ and a_n . Fortunately, it can be verified that (P6) satisfies the time-sharing condition [33], and thus the duality gap becomes negligible when the number of subcarriers is large. Next, (P6) can be optimally solved using the Lagrange duality method. The Lagrangian and its dual function of (P6) are respectively given by

$$\mathcal{L}_{P6} = \sum_{n=1}^M [\Phi_n(a_n, b_{k,n}; \lambda)] - \sum_{k=1}^K \lambda_k P_k, \quad (42)$$

$$g(\lambda) = \inf_{a_n, b_{k,n}} \mathcal{L}_{P6} = \sum_{n=1}^M \underbrace{\inf_{a_n, b_{k,n}} \Phi_n(a_n, b_{k,n}; \lambda)}_{\psi_n(\lambda)} - \sum_{k=1}^K \lambda_k P_k, \quad (43)$$

where $\Phi_n(a_n, b_{k,n}; \lambda) \triangleq \sum_{k=1}^K |1 - a_n h_{k,n} b_{k,n}|^2 \hat{\sigma}_{k,n}^2 + |a_n|^2 \sigma_w^2 + \sum_{k=1}^K \lambda_k \nu_{k,n}^2 |b_{k,n}|^2$ and $\lambda = [\lambda_1, \dots, \lambda_K]^T \succeq \mathbf{0}$ collects the dual variables corresponding to the individual power constraints of the users. For a fixed a_n , minimizing Φ_n w.r.t. $b_{k,n}$ yields

$$|b_{k,n}^*(\lambda_k, a_n)| = \frac{|a_n| |h_{k,n}| \hat{\sigma}_{k,n}^2}{|a_n|^2 |h_{k,n}|^2 \hat{\sigma}_{k,n}^2 + \lambda_k \nu_{k,n}^2}. \quad (44)$$

Substituting (44) back $\Phi_n(a_n, b_{k,n}; \lambda)$ gives

$$\hat{\sigma}_{k,n}^2 |1 - a_n h_{k,n} b_{k,n}^*|^2 + \lambda_k \nu_{k,n}^2 |b_{k,n}^*|^2 = \frac{\lambda_k \nu_{k,n}^2 \hat{\sigma}_{k,n}^2}{\hat{\sigma}_{k,n}^2 |a_n|^2 |h_{k,n}|^2 + \lambda_k \nu_{k,n}^2}.$$

Hence, the dual term for each subcarrier is

$$\psi_n(\lambda) = \min_{a_n} \sum_{k=1}^K \underbrace{\frac{\lambda_k \nu_{k,n}^2 \hat{\sigma}_{k,n}^2}{|a_n|^2 |h_{k,n}|^2 \hat{\sigma}_{k,n}^2 + \lambda_k \nu_{k,n}^2}}_{\phi_n(|a_n|^2; \lambda)} + |a_n|^2 \sigma_w^2.$$

Let $r_n = |a_n|^2 \geq 0$, minimizing $\phi_n(r_n; \lambda)$ w.r.t. r_n yields

$$\sum_{k=1}^K \frac{\lambda_k \nu_{k,n}^2 |h_{k,n}|^2 \hat{\sigma}_{k,n}^4}{(r_n |h_{k,n}|^2 \hat{\sigma}_{k,n}^2 + \lambda_k \nu_{k,n}^2)^2} = \sigma_w^2. \quad (45)$$

which has a unique positive root $r_n^*(\lambda)$. Substituting it into (43) gives

$$g(\lambda) = \sum_{n=1}^N \phi_n(r_n^*(\lambda); \lambda) - \sum_{k=1}^K \lambda_k P_k. \quad (46)$$

Base on (45), (44) and (7), the dual problem can be solved by the subgradient-based methods such as the ellipsoid method [32]. The procedure is summarized in Algorithm 2.

2) *Decision-Optimal Case*: For the decision-optimal case, the objective is to maximize the MD of the received features across all subcarriers. Based on (8) and (37), the corresponding optimization problem can be formulated as

$$(P7) \quad \max_{\{b_{k,n}\}_{n=1}^M} \sum_{n=1}^M G_{\min}(\hat{y}_n), \quad \text{s.t. (7).}$$

Algorithm 2 Dual-Decomposition for (P6)

- 1: **Input**: $\{h_{k,n}\}, \{\sigma_n^2\}, \sigma_w^2, \{\nu_n^2\}, P_k, \varepsilon_\lambda$, and ε_p .
 - 2: **Initialize**: generate $\lambda_k^{(0)} > 0, r_n^{(0)} > 0$; set iteration index $t \leftarrow 0$.
 - 3: **repeat**
 - 4: **(Update per-subcarrier auxiliary)** For each n , solve (45) with given $\{\lambda_k^{(t)}\}$ to obtain $r_n^{(t+1)}$;
 - 5: **(Update per-user dual variable)** For each k , update λ_k using (46) with $\{r_n^{(t+1)}\}$;
 - 6: $t \leftarrow t + 1$;
 - 7: **until** $\max_k |\lambda_k^{(t)} - \lambda_k^{(t-1)}| \leq \varepsilon_\lambda$ **and** power violations in (7) are below ε_p
 - 8: **(Closed-form recovery)** Compute $b_{k,n}^*$ using (44), the final $\{\lambda_k^{(t)}\}$ and $\{r_n^{(t)}\}$.
 - 9: **Output**: $b_{k,n}^*$.
-

(P7) is also non-convex due to the coupling between $b_{k,n}$ across users and subcarriers. Similar to (P6), (P7) satisfies the time-sharing condition, and can thus be solved using the Lagrange duality method. Following the same procedure as in (44) and (45), we have

$$|b_{k,n}^*| = \frac{|\Delta_n|^2 |h_{k,n}| z_n}{\lambda_k \nu_{k,n}^2 + |\Delta_n|^2 \hat{\sigma}_{k,n}^2 |h_{k,n}|^2 z_n^2}, \quad (47)$$

$$\sum_{k=1}^K \frac{\lambda_k |h_{k,n}|^2 \nu_{k,n}^2}{(\lambda_k \nu_{k,n}^2 + |\Delta_n|^2 |h_{k,n}|^2 \hat{\sigma}_{k,n}^2 z_n^2)^2} = \frac{\sigma_w^2}{|\Delta_n|^2}, \quad (48)$$

where the auxiliary variable is introduced as $z_n \triangleq \frac{\sum_{k=1}^K |h_{k,n} b_{k,n}|}{\sum_{k=1}^K |h_{k,n} b_{k,n}|^2 \hat{\sigma}_{k,n}^2 + \sigma_w^2}$. Then, the outer-layer variables λ_k are updated to satisfy the power constraints in (7) based on (47), while the inner layer solves for the optimal z_n^* on each subcarrier according to (48).

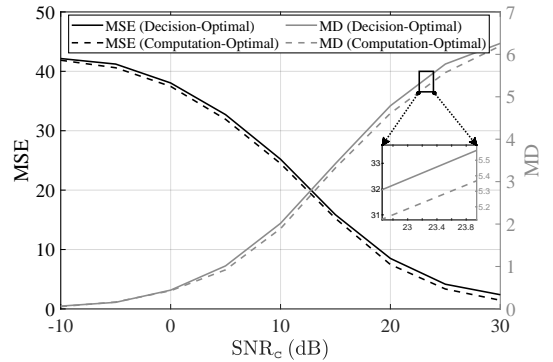


Fig. 5: MSE and MD versus communication SNR under MSE-optimal and decision-optimal designs in the FDM setting.

To provide a deeper insight into the two cases under FDM, we transform (P6) as follows. For fixed $b_{k,n}$, the n -th term of (P6) is quadratic w.r.t. a_n , i.e.,

$$\text{MSE}_n(a_n) = \sum_{k=1}^K |a_n h_{k,n} b_{k,n} - 1|^2 \hat{\sigma}_{k,n}^2 + |a_n|^2 \sigma_w^2, \quad (49)$$

whose minimizer is $|a_n^*(b_{k,n})| = \frac{\sum_{k=1}^K |h_{k,n} b_{k,n}| \hat{\sigma}_{k,n}^2}{\sum_{k=1}^K |h_{k,n} b_{k,n}|^2 \hat{\sigma}_{k,n}^2 + \sigma_w^2}$. Sub-

stituting a_n^* back (49) yields

$$\text{MSE}_n^*(b_{k,n}) = \sum_{k=1}^K \hat{\sigma}_{k,n}^2 - \frac{|\sum_{k=1}^K h_k b_{k,n} \hat{\sigma}_{k,n}^2|^2}{\sum_{k=1}^K |h_k b_{k,n}|^2 \hat{\sigma}_{k,n}^2 + \sigma_w^2}. \quad (50)$$

The term $\sum_{k=1}^K \hat{\sigma}_{k,n}^2$ is independent of $b_{k,n}$, hence minimizing the MSE is equivalent to maximize $\frac{|\sum_{k=1}^K h_k b_{k,n} \hat{\sigma}_{k,n}^2|^2}{\sum_{k=1}^K |h_k b_{k,n}|^2 \hat{\sigma}_{k,n}^2 + \sigma_w^2}$.

Remark 5. By comparing (50) with $G_{\min}(\hat{y}_n)$ in (P7), the key structural difference is the discriminative prior Δ_n . From a Bayesian perspective, decision-optimal design optimizes the conditional discriminant given Δ_n , thereby inducing non-uniform power allocation across different subcarriers. As shown in Fig. 5, although the decision-optimal design yields a higher MSE than the computation-optimal design, it achieves a larger MD. In Section V, we further demonstrate that this MD gain translates into improved downstream inference gain.

V. NUMERICAL RESULTS

In this section, we evaluate the system performance from two aspects: (i) a comparative analysis between the RWB and ML estimators at the sensing level, and (ii) a performance benchmarking of different AirComp transceiver designs at the communication level. These results quantify how the exploitation of prior information enhances inference performance ⁶

A. Settings

1) *Sensing Parameters:* All devices perform $I = 12,000$ sensing observations, forming the dataset, which is divided into training, validation, and test sets in a ratio of 3:1:1. The downstream task is formulated as a five-class human posture classification problem, where each data sample consists of a time–frequency spectrogram derived from FMCW signals [34]. The sensing parameters are configured as follows: carrier frequency 60 GHz, bandwidth 100 MHz, sampling rate 125 MHz, chirp duration 10 μ s, pulse repetition interval 1 ms, and a total of 3,000 pulses per frame. Fig. 6 displays two representative spectrograms corresponding to ‘standing’ and ‘walking’ motions, generated via the Short-Time Fourier Transform (STFT).

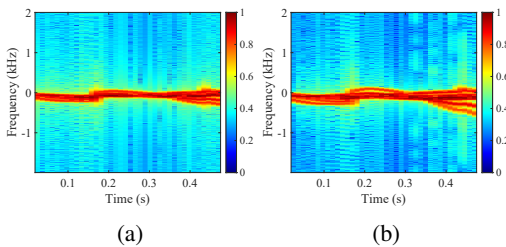


Fig. 6: Two wireless sensing samples of human motion: (a) standing and (b) walking.

⁶The source code, dataset, and well-trained inference model are available online at: https://github.com/dongbiao321/Bayesian_ISEA.

2) *Inference Parameters:* For the inference models, we adopt multilayer perceptron (MLP) and support vector machine (SVM), which are trained on noise-free PCA features extracted from the aforementioned dataset. The SVM adopts the scikit-learn SVC with the default radial basis function [19], penalty with 1, and kernel width with 10^{-3} . The MLP has two hidden layers with sizes 80 and 40, ReLU activation, Adam optimizer, and runs for a maximum of 160 iterations.

3) *System Parameters:* Key system parameters are configured as follows: $\sigma_w^2 = 0.1$, $K = 3$, $M = 4$ and $\{\sigma_k^2\}_{k=1}^K$ are randomly generated to satisfy the target SNR_s. The simulation results are averaged over 1,000 independent Monte Carlo trials.

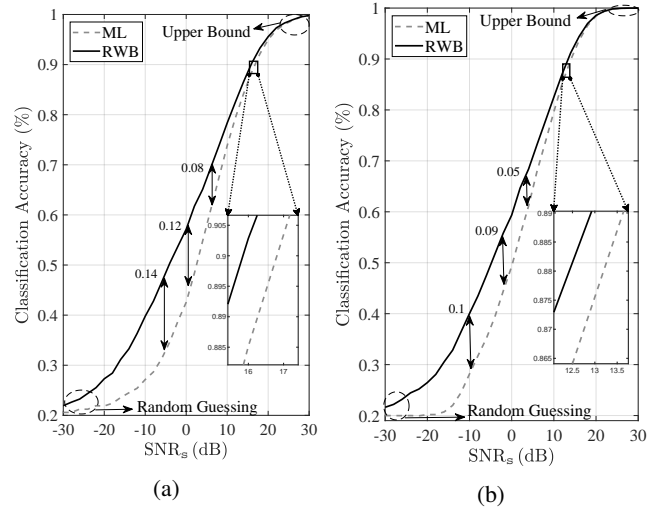


Fig. 7: Classification performance comparison between ML and RWB estimators under different inference models: (a) MLP and (b) SVM.

B. Sensing Level

We first evaluate the inference performance at the sensing level. Fig. 7 illustrates the classification accuracy of the ML and RWB estimators across different inference models. In this evaluation, we consider noise-free aggregation without fading or noise and focus on the impact of the estimators. Two key observations can be drawn from Fig. 7:

- Both SVM and MLP exhibit the trend that the RWB estimator outperforms ML at low SNR. This is because, when the SNR is low, the sensing noise variance σ_k^2 dominates, making the responsibilities θ_ℓ smoother and more heavily influenced by the priors. As a result, the estimator shrinks noisy features toward the class means, thereby reducing within-class uncertainty and enhancing the separability of the decision boundaries. At extremely low SNR levels, the classification performance of both estimators degrades to random guessing, i.e., $1/|\mathcal{L}|$.
- The performance gap between the two estimators gradually narrows, and they converge to the same upper bound at high SNR. This is because, as $\sigma_k^2 \rightarrow 0$, we have $\varrho_k \rightarrow 1$, which implies $\hat{x}_k^{\text{RWB}} \approx \hat{x}_k^{\text{ML}}$, and the responsibilities θ_ℓ concentrates around the true class. Hence, the prior's influence diminishes, and the RWB estimator is asymptotically equivalent to the ML estimator.

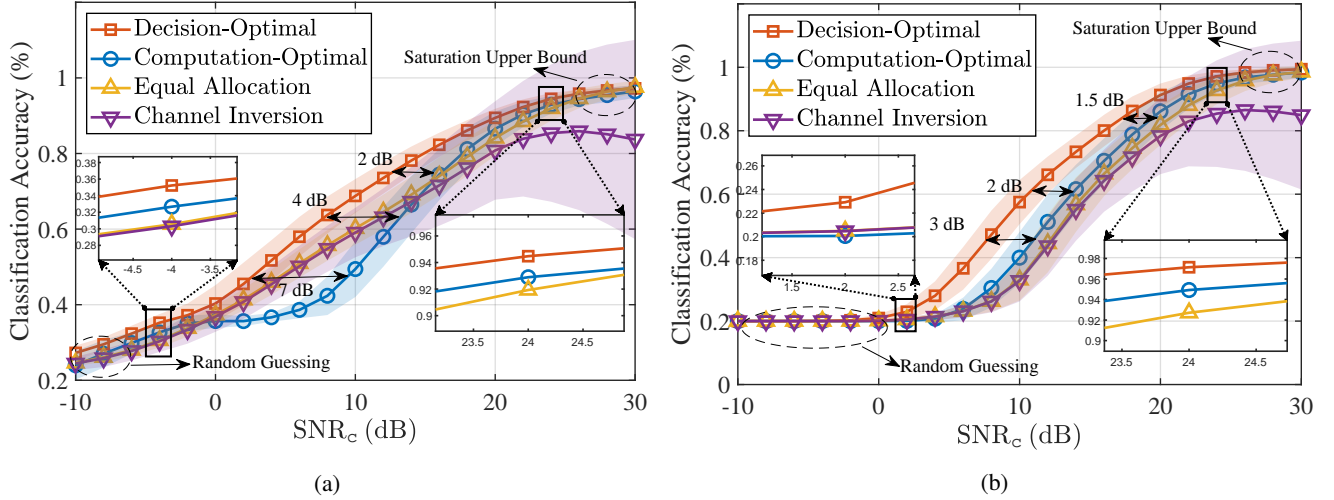


Fig. 8: Classification performance comparison under varying communication SNR: (a) MLP and (b) SVM.

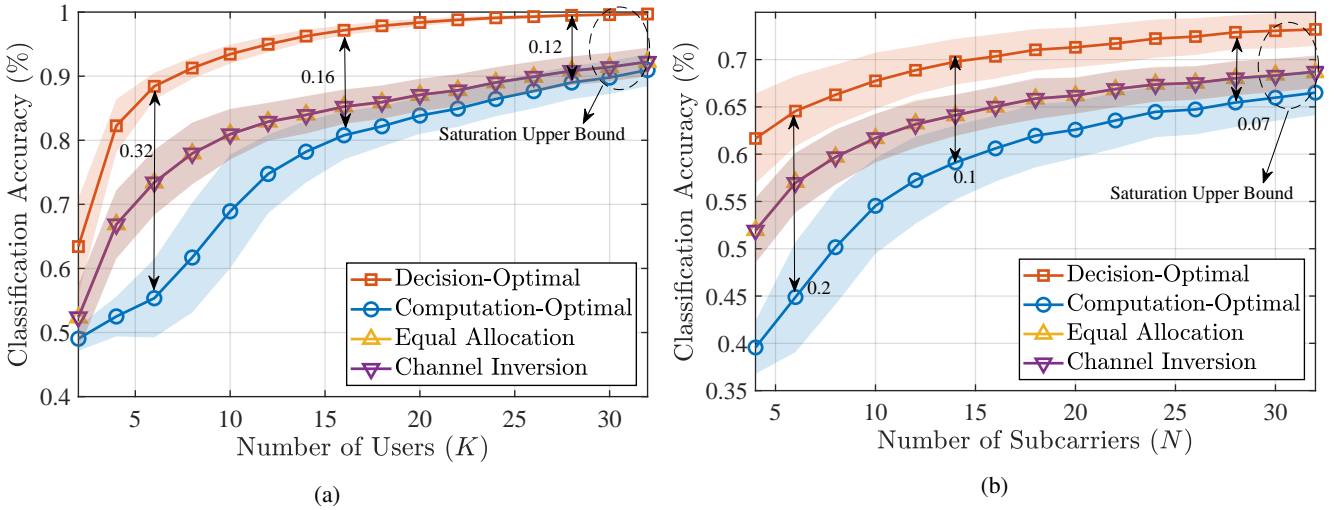


Fig. 9: MLP classification performance comparison under varying number of users K and subcarriers N

Overall, the sensing-level results confirms the superiority of the RWB estimator, which effectively leverages class priors to improve the inference performance at low SNR. In this regime, the prior-induced shrinkage plays a critical role in mitigating class uncertainty. However, as expected, the impact of the prior fades in the high-SNR regime [14].

C. Communication Level

Next, we present the performance evaluation at the communication level. To benchmark the proposed AirComp transceiver designs, we consider two baseline schemes: (1) *Equal Allocation*, with uniform power allocation across all subcarriers, and (2) *Channel Inversion*, with $|b_{k,n}| = \min\{\sqrt{P_k/(N\nu_{k,n}^2)}, 1/|h_{k,n}|\}$.

1) *Classification Performance versus SNR_c*: In Fig. 8, classification performance with $M = N = 4$ is evaluated across a range of communication SNR. The highlighted shadows in the figures represent the standard deviation band across Monte Carlo trials at each SNR, visualizing performance variability

from channel randomness⁷. Three key observations can be made:

- At high SNR levels, all schemes except *Channel Inversion* approach the saturation upper bound. This is because *Channel Inversion* attempts to compensate all subcarriers, but the total power constraint across all subcarriers limits its effectiveness. At extremely low SNR levels, the classification performance of all schemes degrades to random guessing.
- In the moderate-SNR regime (i.e., $[0, 20]$ dB), the decision-optimal scheme yields superior classification accuracy, benefiting from discriminant-aware and non-uniform resource allocation across different features, as stated in Remark 5. Compared with the computation-optimal scheme, it attains the same performance at a lower SNR.

⁷It can be defined as $\bar{m}(p) \pm s(p)$ where $\bar{m}(p) = \frac{1}{T} \sum_{t=1}^T m_t(p)$ and $s(p) = \sqrt{\frac{1}{T-1} \sum_{t=1}^T (m_t(p) - \bar{m}(p))^2}$, with $m_t(p)$ the classification performance in trial t at power p .

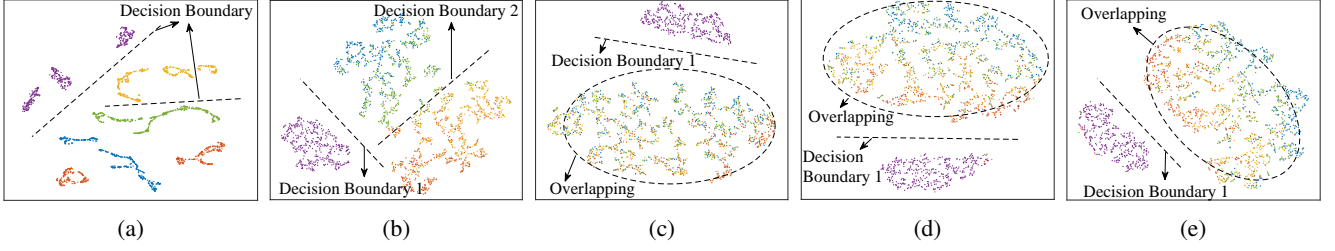


Fig. 10: The feature visualization under different communication schemes: (a) raw features, (b) decision-optimal, (c) computation-optimal, (d) equal allocation, and (e) channel inversion.

- The performance of computation-optimal scheme degrades under MLP. This is because MLP is more sensitive to distributional mismatches between training and test features, whereas SVM determines its parameters via margin-based convex optimization [19], which is generally more robust to such mismatches. As the SNR increases, this mismatch diminishes and the computation-optimal scheme also approaches the performance upper bound. By contrast, the decision-optimal scheme performs task-aware feature scaling that preserves discriminative structure, thereby yielding superior classification performance for both classifiers.

2) *Classification Performance versus K* : In Fig. 9(a), MLP classification performance is evaluated under varying numbers of users K with $\text{SNR}_c = 10$ dB and $M = N = 4$. The results validate Theorem 2, showing that with sufficient independent observations in aggregation, the class uncertainty decreases accordingly. As K increases, all schemes converge to their asymptotic upper bounds. Moreover, the performance gap between the computation-optimal and decision-optimal schemes gradually shrinks, since the aggregation error vanishes with large K .

3) *Classification Performance versus N* : In Fig. 9(b), classification performance under different numbers of subcarriers N with $\text{SNR}_c = 10$ dB, $M = 4$ and $K = 3$ is presented. Similar to the case with varying K , the performance gap between the decision-optimal and computation-optimal schemes gradually narrows as N increases. However, the underlying reason here is different: as N grows, the heterogeneity of the effective channels diminishes, causing both schemes to approach their respective time-sharing bounds.

4) *Visualization Analysis*: Fig. 10 visualizes the feature distributions under different AirComp transceiver designs. Specifically, t-SNE is employed to project the features from the original high-dimensional space onto a two-dimensional plane [35]. Fig. 10 shows that the decision-optimal scheme yields more clear inter-class separation. For example, the decision-optimal scheme reveals two distinct decision boundaries between clusters, indicating richer separability for the classification task, whereas the other schemes exhibit essentially a single dominant decision boundary with noticeable cluster overlapping. Regarding the detailed classification behavior of each class, the confusion matrices in Fig. 11 show that the decision-optimal scheme achieves more uniform class-wise discrimination. These results verify that employing a discriminative prior effectively increases inter-class separation.

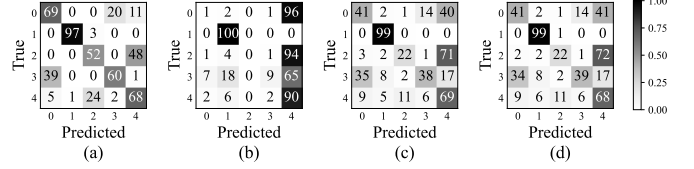


Fig. 11: MLP confusion matrices with $\text{SNR}_c = 10$ dB under different communication schemes: (a) decision-optimal, (b) computation-optimal, (c) equal allocation, and (d) channel inversion.

In summary, the communication-level results demonstrate that the decision-optimal scheme enhances inference performance by incorporating a discriminative prior into the transceiver design. The performance gap between the computation-optimal and decision-optimal schemes is characterized across different system parameters (SNR_c , K and N), revealing distinct performance bounds and scaling behaviors.

VI. CONCLUSION

This paper investigates a distributed ISEA system under a Bayesian framework, focusing on incorporating task-relevant priors to maximize inference performance. At the sensing level, an RWB estimator with a GM prior is designed. By weighting class-conditional posterior means with responsibilities, RWB effectively denoises features and outperforms ML at low SNR. At the communication level, two theoretical proxies are introduced: the computation-optimal and decision-optimal proxies. Optimal transceiver designs in terms of closed-form power allocation are derived for both TDM and FDM settings, revealing threshold-based and dual-decomposition structures. Results show that the discriminant-aware allocation yields additional inference gains.

REFERENCES

- [1] B. Dong and B. Cao, "Optimized power control for multi-user integrated sensing and edge AI," in *Proc. IEEE Int. Conf. Commun. (ICC)*, Glasgow, U.K., May 2026, submitted.
- [2] F. Liu, Y. Cui, C. Masouros, J. Xu, T. X. Han, Y. C. Eldar, and S. Buzzi, "Integrated sensing and communications: Toward dual-functional wireless networks for 6G and beyond," *IEEE J. Sel. Areas Commun.*, vol. 40, no. 6, pp. 1728–1767, 2022.
- [3] M. Ma, C. Gong, L. Zeng, Y. Yang, and L. Wu, "Floccoff: Data heterogeneity resilient federated learning with communication-efficient edge offloading," *IEEE J. Sel. Areas Commun.*, 2024.
- [4] B. Dong, B. Cao, G. Gui, and Q. Zhang, "Robust deep joint source-channel coding enabled distributed image transmission with imperfect channel state information," *IEEE Trans. Wireless Commun.*, early access, Sep. 2025.

- [5] D. Wen, P. Liu, G. Zhu, Y. Shi, J. Xu, Y. C. Eldar, and S. Cui, "Task-oriented sensing, computation, and communication integration for multi-device edge AI," *IEEE Trans. Wireless Commun.*, vol. 23, no. 3, pp. 2486–2502, 2023.
- [6] Z. Liu, X. Chen, H. Wu, Z. Wang, X. Chen, D. Niyato, and K. Huang, "Integrated sensing and edge AI: Realizing intelligent perception in 6G," *IEEE Comm. Surv. Tutor.*, early access, May 2025.
- [7] D. Wen, X. Jiao, P. Liu, G. Zhu, Y. Shi, and K. Huang, "Task-oriented over-the-air computation for multi-device edge AI," *IEEE Trans. Wireless Commun.*, vol. 23, no. 3, pp. 2039–2053, 2023.
- [8] X. Chen, K. B. Letaief, and K. Huang, "On the view-and-channel aggregation gain in integrated sensing and edge AI," *IEEE J. Sel. Areas Commun.*, vol. 42, no. 9, pp. 2292–2305, 2024.
- [9] X. Mu and Y. Liu, "Exploiting semantic communication for non-orthogonal multiple access," *IEEE J. Sel. Areas Commun.*, vol. 41, no. 8, pp. 2563–2576, 2023.
- [10] B. Dong, B. Cao, and Q. Zhang, "Inference-optimal ISAC via task-oriented feature transmission and power allocation," *arXiv preprint arXiv:2510.20429*, 2025.
- [11] A. Şahin and R. Yang, "A survey on over-the-air computation," *IEEE Comm. Surv. Tutor.*, vol. 25, no. 3, pp. 1877–1908, 2023.
- [12] X. Cao, G. Zhu, J. Xu, and K. Huang, "Optimized power control for over-the-air computation in fading channels," *IEEE Trans. Wireless Commun.*, vol. 19, no. 11, pp. 7498–7513, 2020.
- [13] W. Liu, X. Zang, Y. Li, and B. Vucetic, "Over-the-air computation systems: Optimization, analysis and scaling laws," *IEEE Trans. Wireless Commun.*, vol. 19, no. 8, pp. 5488–5502, 2020.
- [14] S. M. Kay, *Fundamentals of statistical signal processing: Estimation theory*. Prentice-Hall, Inc., 1993.
- [15] C. Cai, X. Yuan, and Y.-J. A. Zhang, "End-to-end learning for task-oriented semantic communications over MIMO channels: An information-theoretic framework," *IEEE J. Sel. Areas Commun.*, vol. 43, no. 4, pp. 1292–1307, 2025.
- [16] B. S. Clarke and A. R. Barron, "Information-theoretic asymptotics of Bayes methods," *IEEE Trans. Inf. Theory*, vol. 36, no. 3, pp. 453–471, 2002.
- [17] Z. Liu, Q. Lan, A. E. Kalør, P. Popovski, and K. Huang, "Over-the-air multi-view pooling for distributed sensing," *IEEE Trans. Wireless Commun.*, vol. 23, no. 7, pp. 7652–7667, 2023.
- [18] J. Yao, W. Xu, G. Zhu, K. Huang, and S. Cui, "Energy-efficient edge inference in integrated sensing, communication, and computation networks," *IEEE J. Sel. Areas Commun.*, early access, May 2025.
- [19] C. M. Bishop and N. M. Nasrabadi, *Pattern recognition and machine learning*. New York, USA: Springer Science & Business Media, 2006.
- [20] B. Dong, B. Cao, and Q. Zhang, "Lightweight semantic-aware communication with packet transmission," *IEEE Commun. Lett.*, vol. 29, no. 7, pp. 1569–1573, 2025.
- [21] A. Assa and K. N. Plataniotis, "Wasserstein-distance-based Gaussian mixture reduction," *IEEE Signal Process. Lett.*, vol. 25, no. 10, pp. 1465–1469, 2018.
- [22] D. Tse and P. Viswanath, *Fundamentals of wireless communication*. Cambridge, U.K.: Cambridge Univ. Press, 2005.
- [23] A. Carleial, "Interference channels," *IEEE Trans. Inf. Theory*, vol. 24, no. 1, pp. 60–70, 2003.
- [24] T. K. Moon, "The expectation-maximization algorithm," *IEEE Signal Process. Mag.*, vol. 13, no. 6, pp. 47–60, 1996.
- [25] T. M. Cover, *Elements of information theory*. John Wiley & Sons, 1999.
- [26] G. H. Hardy, J. E. Littlewood, and G. Pólya, *Inequalities*, 2nd ed. Cambridge, U.K.: Cambridge Univ. Press, 1952.
- [27] J. Sokolić, R. Giryes, G. Sapiro, and M. R. Rodrigues, "Robust large margin deep neural networks," *IEEE Trans. Signal Process.*, vol. 65, no. 16, pp. 4265–4280, 2017.
- [28] F. Kanaya *et al.*, "The asymptotics of posterior entropy and error probability for Bayesian estimation," *IEEE Trans. Inf. Theory*, vol. 41, no. 6, pp. 1988–1992, 1995.
- [29] K. Fukunaga, *Introduction to statistical pattern recognition*. Amsterdam, The Netherlands: Elsevier, 2013.
- [30] Q. Lan, Q. Zeng, P. Popovski, D. Gündüz, and K. Huang, "Progressive feature transmission for split classification at the wireless edge," *IEEE Trans. Wireless Commun.*, vol. 22, no. 6, pp. 3837–3852, 2022.
- [31] E. Kreyszig, *Introductory functional analysis with applications*. John Wiley & Sons, 1991.
- [32] S. P. Boyd and L. Vandenberghe, *Convex optimization*. Cambridge, U.K.: Cambridge Univ. Press, 2004.
- [33] W. Yu and R. Lui, "Dual methods for nonconvex spectrum optimization of multicarrier systems," *IEEE Trans. Wireless Commun.*, vol. 54, no. 7, pp. 1310–1322, 2006.
- [34] G. Li, S. Wang, J. Li, R. Wang, X. Peng, and T. X. Han, "Wireless sensing with deep spectrogram network and primitive based autoregressive hybrid channel model," in *Proc. IEEE Int. Workshop Signal Process. Adv. Wireless Commun. (SPAWC)*, Sep. 2021, pp. 481–485.
- [35] L. Van der Maaten and G. Hinton, "Visualizing data using t-SNE," *J. Mach. Learn. Res.*, vol. 9, no. Nov, pp. 2579–2605, 2008.